

Component-dependent thermal properties of molten salt eutectics for solar thermal energy storage: experiments, molecular simulation and applications

Shuai Zhang^a, Ziyuan Li^b, Huan Wang^b, Limei Tian^b, Yingai Jin^c, Mark Alston^a, Yuying Yan^{a,}*

^a Faculty of Engineering, University of Nottingham, University Park, Nottingham, UK

^b Key Laboratory of Bionic Engineering (Ministry of Education), Jilin University, Changchun, China

^c State Key Laboratory of Automotive Simulation and Control, Jilin University, Changchun, China

* Corresponding author, E-mail: Yuying.Yan@nottingham.ac.uk

ABSTRACT

Molten salts have been used in solar thermal energy storage due to their high energy storage density, low cost and excellent chemical stability. However, their application is limited by “bad days” such as cloudy days and winter because the weak concentrated solar radiation cannot melt the salt. The current study indicates that through mixing pure salts, the melting point of molten salt can be decreased significantly while the latent heat is not impaired. This is very important for solar thermal energy storage systems on “bad days” because the system using the low-melting-point salt is still possible to work on these days. The case study was performed in Nottingham, the United Kingdom and Dezhou, China respectively. The pure salt and salt mixture were used as the heat transfer fluid and energy storage medium in the solar tower power plant. It is found that by using the low-melting-point salt eutectic, the yearly operation time of the plant is increased by 75 days for Dezhou and 33 days for Nottingham. In addition, a molecular simulation was performed to reveal the mechanism underlying the component-dependent thermal properties. Mixing pure salts is proved to be a simple method to improve the utilization efficiency of the solar power plant.

Keywords: molten salt; eutectic; low melting point; molecular simulation; solar thermal energy storage

1. Introduction

Using solar energy is an effective method to cope with the global energy crisis and environmental pollution [1-3]. To address the intermittence issue, solar thermal energy storage (STES) is proposed [4-6]. This technique collects solar energy during the day and stores it in phase change materials (PCMs) in the form of thermal energy; at night, the stored solar thermal energy is released for house heating, power generation etc. [7, 8].

Molten salts are the most common energy storage medium for STES due to their high energy storage density, low cost, low vapour pressure and excellent chemical stability [9]. The molten salt absorbs solar thermal energy and undergoes the phase change, which stores thermal energy in the form of latent heat; meanwhile, its temperature increases, which stores thermal energy in the form of sensible heat. In addition, the liquid salt acts as the heat transfer fluid (HTF) and is used to heat the steam in the heat exchanger [10]. The mixed molten salts such as the solar salt (60wt% NaNO_3 + 40wt% KNO_3) are commonly used as the energy storage medium [11]. Since thermal properties are critical considerations for selecting PCMs, some researchers have studied the thermal properties of mixed molten salts. Coscia et al. [12] investigated the viscosity, specific heat and latent heat of LiNO_3 - NaNO_3 - KNO_3 mixture. They found that the viscosity of the ternary mixture was almost identical to that of 50:50 mol% NaNO_3 - KNO_3 . LiNO_3 has the highest specific heat and latent heat among the three nitrates, thus the specific heat of the ternary mixture increases with the increasing LiNO_3 component. Unexpectedly, although the latent heat of the ternary mixture is higher than that of the NaNO_3 - KNO_3 mixture, the increasing LiNO_3 component does not result in higher latent heat. The melting point of the ternary mixture is lower than that of each component. Anagnostopoulos et al. [13] used the molecular dynamics (MD) simulation to compute the density, thermal conductivity, self-diffusivity, viscosity and surface tension of NaNO_3 - KNO_3 mixtures (59.6%-40.4%, 50%-50% and 40.4%-59.6%). Their results indicate that at the decomposition

temperature (450°C), the thermal conductivity of the mixture increases with the increasing KNO₃ ratio. And 50%-50% NaNO₃-KNO₃ has the highest viscosity.

TES technique has been integrated with the concentrated solar power (CSP) plant to ensure the stable power output. In 2010, Medrano et al. [14] reviewed several case studies of solar power plant using TES system. Later, Powell and Edgar [15] simulated a parabolic trough CSP plant with TES. In their research, a two-tank-direct method was used. It is found that adding a storage system increases the solar share of power generation by 47% and reduces the supplementary fuel consumption by 43%. Grange et al. [16] modelled a hybrid solar gas turbine solar plant featuring a TES unit. Their results indicate that the integration of the TES unit offers a higher and more stable electrical generation. Mostafavi Tehrani and Taylor [17] used molten salt as energy storage medium and analysed the performance of a CSP plant in design/off-designed point. Khandelwal et al. [18] reviewed the developments in CSP technologies, heat transfer fluids and phase change materials used for thermal energy storage. Later, they numerically studied an integrated solar thermal cycle with the molten salted-based thermal storage [19]. A mathematical model was developed to analyse the thermo-economic performance of the integrated system. They found that the integration of the solar field with two-tank thermal energy storage improved the power cycle efficiency by up to 40%. They also compared the effect of different heat transfer fluids on the performance of solar cycles [20].

However, solar radiation is not uniform in a year. In winter or cloudy days, the solar radiation is weak, the concentrated sunlight may be not able to melt salt. As a result, solid salt would block the pipeline and the power plant cannot operate. These “bad days” decrease the yearly operation time of the power plant. So, it is desirable that the melting point of molten salt would be low; meanwhile, the energy storage density is guaranteed. Thus in winter or cloudy days, the concentrated solar radiation is still possible to melt the salt to store solar energy and

transfer heat. However, there is little literature considering the effect of weather throughout a year on the operability of the solar power plant and the corresponding solutions.

In the current study, a simple method - mixing pure salts was proposed to decrease the melting point of molten salt. The binary nitrate salts ($\text{NaNO}_3\text{-KNO}_3$) with different component ratios were tested. Moreover, a molecular simulation was performed to reveal the mechanism underlying the variation of thermal properties from the atomic point of view. Finally, a case study was performed in Nottingham, the UK and Dezhou, China to examine the performance of the molten salt mixture. This paper systematically investigated the effect of components on melting point and latent heat of molten salts, from the experiment and atomic point of view. Moreover, a simple method was proposed and proved to improve the utilization efficiency of the solar power plant.

2. Experiments

NaNO_3 and KNO_3 were employed in the experiment. The mole ratio of samples is listed in **Table 1** and the photograph is shown in **Figure 1**. The preparation of $\text{NaNO}_3\text{-KNO}_3$ eutectics is as follows: first, the pure NaNO_3 and KNO_3 were weighed and mixed together, followed by the full dissolution in the excess distilled water; then the solution was dried at 150°C for more than 48 h; finally, the samples were ground for the differential scanning calorimetry (DSC) measurement.

Table 1

Nitrate salts employed in the experiment

No.	Name	Mole ratio of NaNO_3
0#	$\text{Na}_0\text{-K}_1$	0
1#	$\text{Na}_{0.1}\text{-K}_{0.9}$	0.1
2#	$\text{Na}_{0.2}\text{-K}_{0.8}$	0.2
3#	$\text{Na}_{0.3}\text{-K}_{0.7}$	0.3
4#	$\text{Na}_{0.4}\text{-K}_{0.6}$	0.4

5#	$\text{Na}_{0.5}\text{-K}_{0.5}$	0.5
6#	$\text{Na}_{0.6}\text{-K}_{0.4}$	0.6
7#	$\text{Na}_{0.7}\text{-K}_{0.3}$	0.7
8#	$\text{Na}_{0.8}\text{-K}_{0.2}$	0.8
9#	$\text{Na}_{0.9}\text{-K}_{0.1}$	0.9
10#	$\text{Na}_1\text{-K}_0$	1



Figure 1. Photograph of nitrate salts used in the experiment. From left to right is sample 0#, 1#, ..., 10#.

The DSC measurement was performed using Discovery DSC25 (TA Instruments, USA). The accuracy of the temperature control is $\pm 0.01^\circ\text{C}$. The accuracy of the calorimeter (indium, the standard metal) is $\pm 0.1\%$. The baseline reproducibility is $< 40 \mu\text{W}$. Before the DSC measurement, the instrument was calibrated using the standard metal. An approximate 10 mg sample was placed in the alumina crucible while the empty crucible act as the reference. The sample was first heated to 150°C and then subjected to a heating-cooling cycle with a rate of $6^\circ\text{C}/\text{min}$. The first cycle was discarded and the data was acquired from the second cycle. Each sample was tested at least three times.

3. Theoretical modelling

A molecular dynamics simulation was performed to understand the variation of thermal properties from atomic point of view. The simulated system consists of 5040 atoms. The initial crystal structure is obtained from Ref. [21]. Then the cell is replicated to generate the final geometry. The mole ratio of NaNO₃/KNO₃ is the same as that in the experiment.

The Buckingham potential is used to reproduce the pairwise interaction between atoms [22, 23]:

$$E_{buck} = Ae^{-r/\rho} - \frac{C}{r^6} \quad (1)$$

where r is the distance between two atoms; A , ρ and C are Buckingham parameters.

The intra-molecular force field is used to describe the force within the nitrate ion, where the bond stretching is computed as [21]:

$$V_b = k_b (r - r_0)^2 \quad (2)$$

angle bending is computed as:

$$V_\theta = k_\theta (\theta - \theta_0)^2 \quad (3)$$

improper motion is computed as:

$$V_\psi = k_\psi (\psi - \psi_0)^2 \quad (4)$$

Coulombic interaction is computed as:

$$E_{coul} = \frac{q_i q_j}{r} \quad (5)$$

where q_i and q_j are the charge of ions i and j .

The parameters of Buckingham potential are provided in **Table 2**.

Table 2

Buckingham potential parameters for NaNO₃ and KNO₃ [21]

	q/e	$A/\text{kcal mol}^{-1}$	$\rho/\text{\AA}$	$C/\text{kcal mol}^{-1} \text{\AA}^6$
Na	+1	9778.06	0.3170	24.18

K	+1	35833.47	0.3370	349.9
N	+0.95	33652.75	0.2646	259.1
O	-0.65	62142.9	0.2392	259.4
<hr/>				
N-O	$k_b / \text{kcal mol}^{-1} \text{ \AA}^{-2} = 525.0$		$r_o / \text{ \AA} = 1.2676$	
O-N-O	$k_\theta / \text{kcal mol}^{-1} \text{ rad}^{-2} = 105.0$		$\theta_0 / ^\circ = 120.0$	
O-N-O-O	$k_\psi / \text{kcal mol}^{-1} \text{ rad}^{-2} = 60.0$		$\Psi_0 / ^\circ = 0.0$	

For different types of atoms (such as Na and N), the pair coefficient is generated by the following mixing rules [22]:

$$A_{ij} = \sqrt{A_{ii} \cdot A_{jj}} \quad (6)$$

$$C_{ij} = \sqrt{C_{ii} \cdot C_{jj}} \quad (7)$$

$$\frac{1}{\rho_{ij}} = \frac{1}{\rho_{ii}} + \frac{1}{\rho_{jj}} \quad (8)$$

All the simulations were performed using the open-source MD software LAMMPS. The Buckingham and Coulombic interactions were truncated at 11 \AA , with the long-range corrections being applied [21]. The particle-particle-particle-mesh (pppm) solver was used to compute long-range Coulombic interactions. Newton's motion equations were solved through the Verlet algorithm with a time step of 1 fs [10].

The system was firstly subjected to an energy minimization. Then it was equilibrated in the NPT ensemble for 2 ns to relax the system to the desired pressure and temperature [22]. The pressure was fixed as 0.1 MPa while the temperature ranged from 300 K to 800 K, so both the solid and liquid state can be covered. The temperature increment is 50 K; near the melting point, it is set as 10 K. During the simulation process, Nose-Hoover thermostat and barostat were employed to control the pressure and temperature.

In all the simulations, we adopted the “multi constant temperature” method rather than the “gradually heating and cooling” method so that the system can be equilibrated at each specific temperature for a long enough time [24].

4. Results and discussions

4.1 Melting point

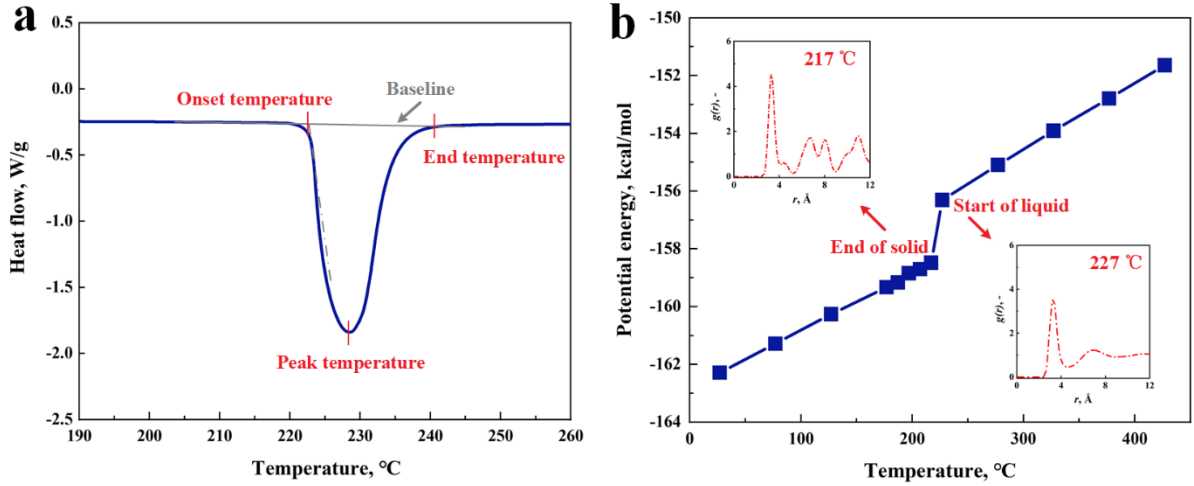


Figure 2. Determining the melting point of $\text{Na}_{0.5}\text{-K}_{0.5}$ using (a) DSC measurement and (b) MD simulation. The inset is the Na-N radial distribution function at T_{solid} (217 °C) and T_{liquid} (227 °C) where T_{solid} and T_{liquid} represent the temperature of the end of solid state and the start of liquid state.

The schematic of determining the melting point using the DSC curve and potential energy curve is shown in **Figure 2**. For the DSC method, three melting temperatures are identified: the extrapolated onset temperature, peak temperature and end temperature [25]. For the MD method, the melting point is determined by the jump in the potential energy curve [26]. It is noted that in Figure 2(b), the potential energy of $\text{Na}_{0.5}\text{-K}_{0.5}$ jumps at 217 °C; the eutectic shows the solid characteristic, as seen from the Na-N radial distribution function (RDF). At 227 °C, the jump ends, and the eutectic shows the liquid feature, indicating the eutectic has molten completely. Here, the temperature where the jump starts is denoted as T_{solid} which means the end of the solid state; the temperature where the jump ends is denoted as T_{liquid} which means the start of the liquid state. For the $\text{Na}_{0.5}\text{-K}_{0.5}$, T_{solid} and T_{liquid} are 217 °C and 227 °C respectively.

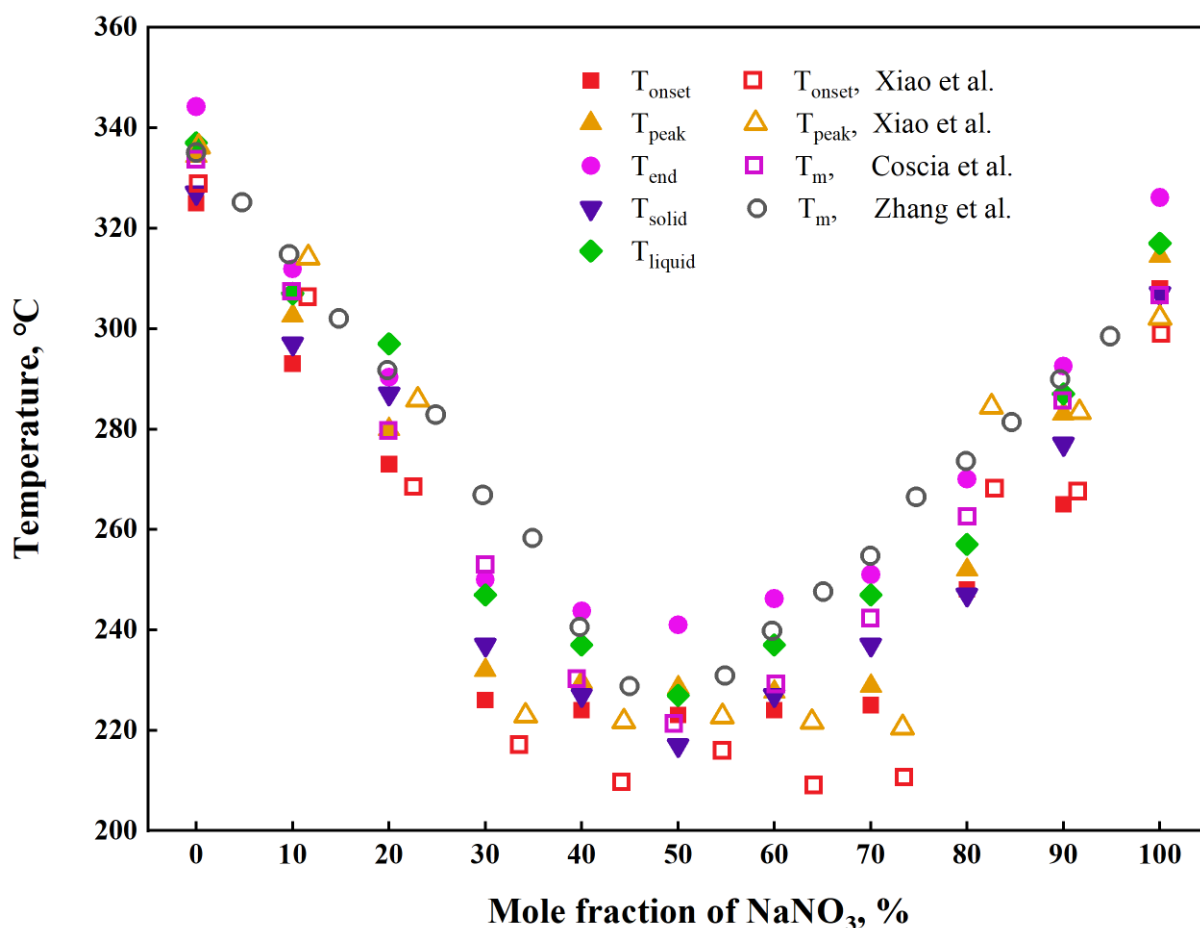


Figure 3. Melting point determined by the experiment and molecular simulation. The literature data are from Xiao et al. [27], Coscia et al. [28] and Zhang et al. [29].

The melting point determined by the DSC curve and MD simulation is presented in **Figure 3**. It is seen that the pure NaNO₃ and KNO₃ have the highest melting point. And the melting point first decreases and then increases with the increasing ratio of NaNO₃, but the melting point of salt mixtures is lower than that of each component. The melting point in the literature [27-29] is also plotted in Figure 3 and they show the same trend.

Our results indicate that Na_{0.5}-K_{0.5} has the lowest melting point and the decrease in melting point is up to 102 °C compared with pure salt. To understand the component-dependent melting point, the structure of nitrate salts was analysed. The nitrate salt is a type of ionic crystal [30]. Na⁺/K⁺ are bonded with NO₃⁻ by the coulombic force, as shown in **Figure 4**. The coulombic force is the attractive force because the charge of Na⁺/K⁺ and NO₃⁻ are opposite. From the atomic point of view, the melting process is that, as the temperature increases, Na⁺, K⁺ and NO₃⁻

vibrate more intensively until they overcome the coulombic force and escape from the lattice point [31]. The coulombic force acts as the resistance for melting.

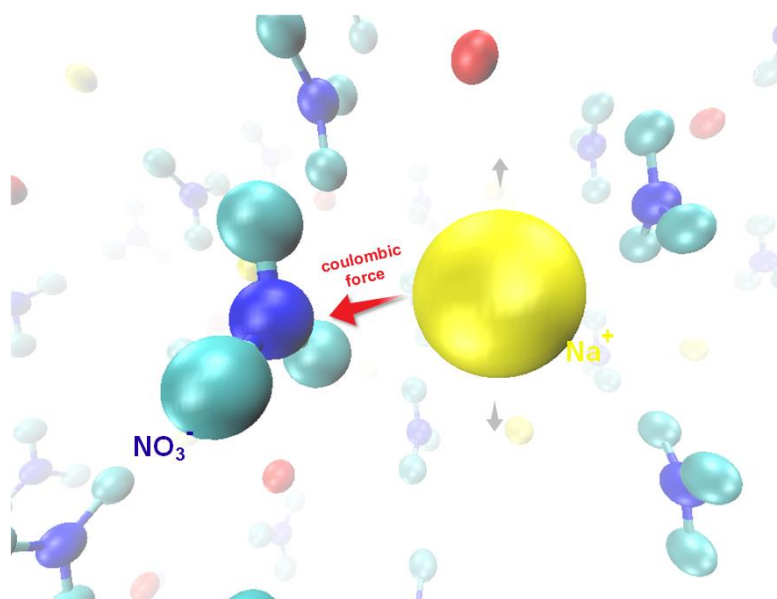


Figure 4. Schematic of the coulombic interaction in NaNO₃/KNO₃ eutectic. Yellow, red, blue and cyan spheres represent Na, K, N and O atoms respectively.

The coulombic energy computed from the MD simulation is presented in **Figure 5**. It is seen that Na_{0.5}-K_{0.5} has the smallest coulombic energy. This suggests that the “resistance” for melting of Na_{0.5}-K_{0.5} is small, so Na⁺, K⁺ and NO₃⁻ can shake out of the lattice point at a relatively low temperature, which may be responsible for the lowest melting point.

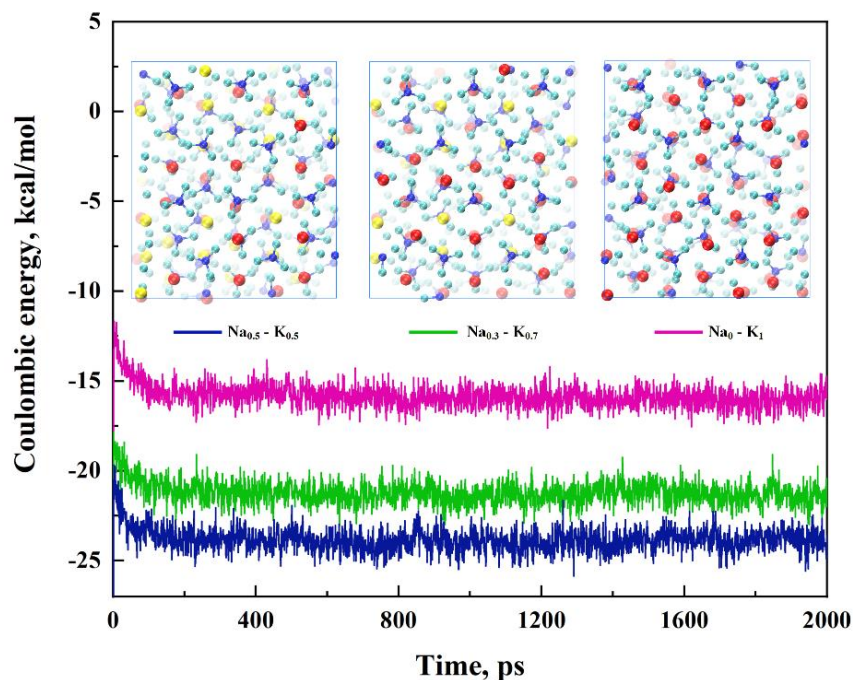


Figure 5. Computed coulombic bonding energy of $\text{Na}_0\text{-K}_1$, $\text{Na}_{0.3}\text{-K}_{0.7}$ and $\text{Na}_{0.5}\text{-K}_{0.5}$. Yellow, red, blue and cyan spheres represent Na, K, N and O atoms respectively.

4.2 Latent heat

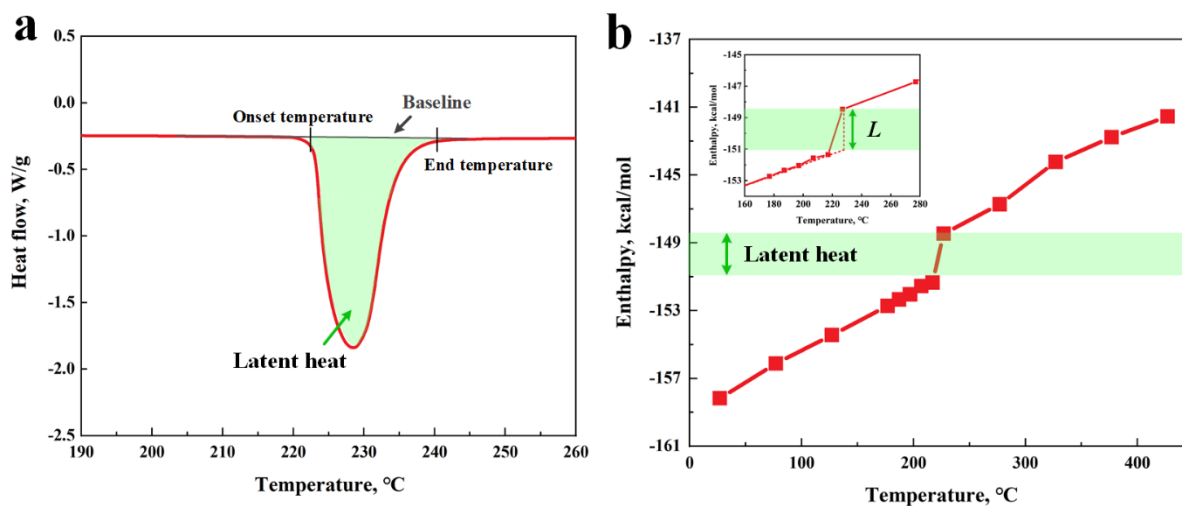


Figure 6. Determining the latent heat of $\text{Na}_{0.5}\text{-K}_{0.5}$ using (a) DSC method and (b) molecular simulation method. The inset shows the determined latent heat where the specific heat is extracted. “ L ” refers to “Latent heat”.

The DSC curve shows the power difference between the tested and the reference sample. Since the empty crucible is used as the reference in the current experiment, the DSC curve indicates the amount of energy required by salt to reach the set temperature. The schematic of

determining the latent heat using the DSC curve is presented in **Figure 6(a)**. The latent heat is obtained by integrating the area between the DSC curve and the baseline from the onset temperature to the end temperature [25]. Actually, the latent heat obtained by this method is the “pure” latent heat because the specific heat has been extracted. It reflects the energy increment induced by the phase change.

The MD method determines the latent heat by identifying the jump in the enthalpy curve. Before melting, the enthalpy increases stably with temperature, which is mainly due to the specific heat. When the temperature reaches the melting point, the phase change occurs and the enthalpy jumps due to the phase change. The latent heat is obtained by computing the enthalpy difference before/after melting. The specific heat is extracted by extrapolating the enthalpy curve to T_{liquid} .

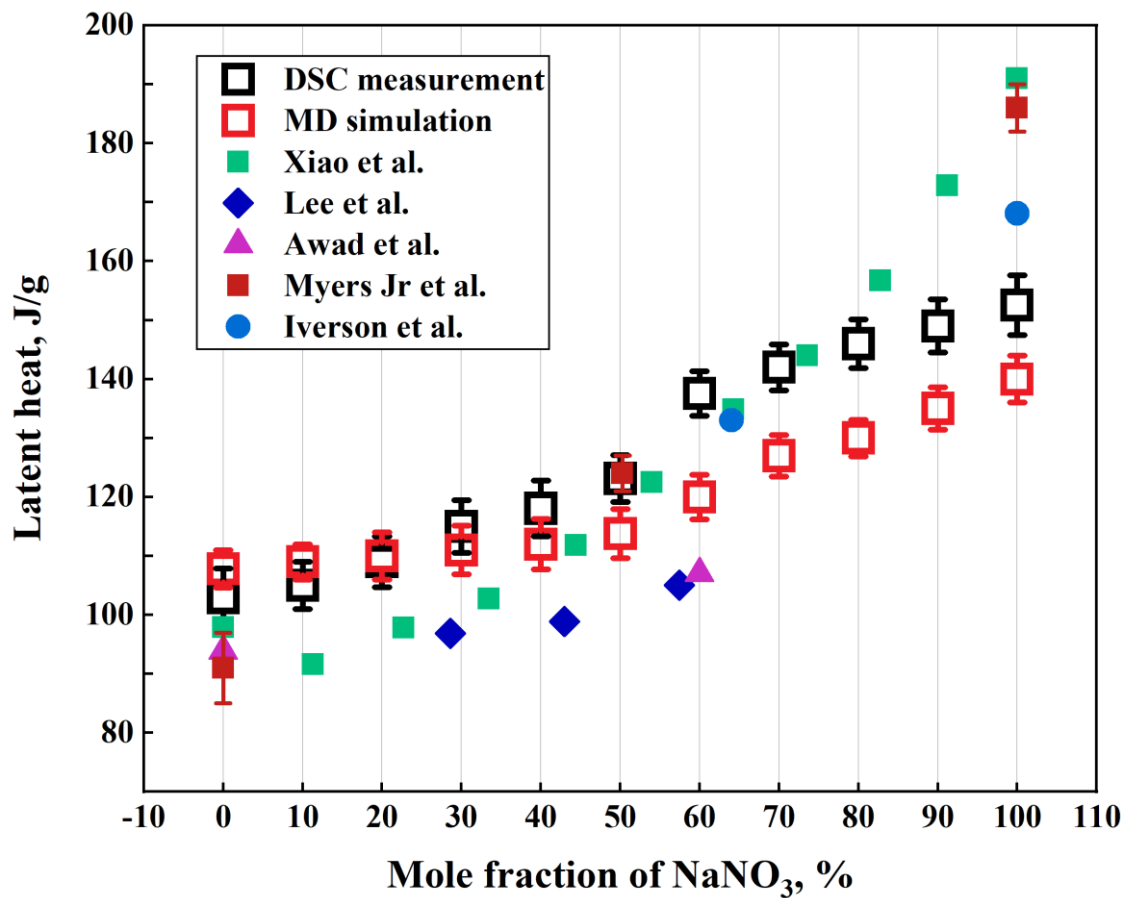


Figure 7. Latent heat determined by DSC measurement and MD simulation. The literature data are from Xiao et al. [27], Lee and Jo [32], Awad et al. [33], Myers Jr et al. [34] and Iverson et al. [35].

The latent heat of nitrate salts is presented in **Figure 7**. Different from the melting point, the latent heat increases with the increasing ratio of NaNO_3 . It is proportional to the component. The latent heat in the literature shows the same trend. The variation of latent heat with components is very important because through mixing pure salts, the melting point of the mixture is decreased while the energy storage density is not impaired.

Latent heat is the energy difference before/after melting. Since the property of matter is determined by its structure, the component-dependent latent heat is explained from the salt structure. The initial structure of NaNO_3 is regular, as shown in **Figure 8**. Na^+ and NO_3^- are located at the lattice point and the structure has the characteristic of “point by point”. At the solid state, atoms vibrate “in place”; although the structure becomes a bit disordered compared with the initial structure, Na^+ and NO_3^- are still locked near the lattice point. The structure is overall “point by point”. However, after melting, Na^+ and NO_3^- distribute randomly; the structure is quite disordered.

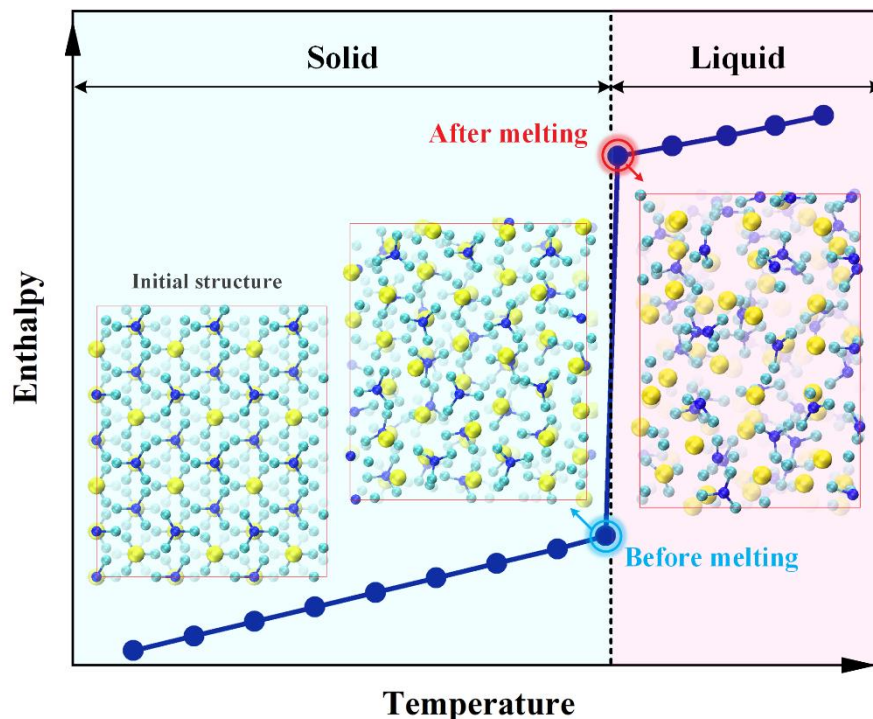


Figure 8. Schematic of the structure of NaNO_3 before/after melting. Yellow, blue and cyan spheres represent Na, N and O atoms respectively.

The coordination number describes the number of atoms surrounding the central atom. It is calculated by [10]:

$$N = 4\pi\rho_{\beta} \int_0^r g_{\alpha\beta}(r)r^2 dr \quad (9)$$

where α and β denote α -type and β -type atom, respectively; ρ_{β} is the number density of β -type atom; r is the distance between α -type and β -type atoms; $g_{\alpha\beta}$ is the radial distribution function.

Taking $r = r_{\min}$ (r_{\min} is the first valley position of the RDF curve), the coordination number is obtained. **Figure 9** shows the coordination number curves of $\text{Na}_1\text{-K}_0$, $\text{Na}_{0.5}\text{-K}_{0.5}$, and $\text{Na}_0\text{-K}_1$. The temperature of “before melting” and “after melting” for $\text{Na}_1\text{-K}_0$, $\text{Na}_{0.5}\text{-K}_{0.5}$, and $\text{Na}_0\text{-K}_1$ is 580 K and 590 K, 490 K and 500 K, 600 K and 610 K respectively. The first valley position of the RDF curves is located at around 4.75 Å. It is seen that the difference in coordination number before/after melting is $\text{Na}_1\text{-K}_0$, $\text{Na}_{0.5}\text{-K}_{0.5}$, and $\text{Na}_0\text{-K}_1$ in order from large to small. The larger the difference in coordination number, the greater the change in the local structure, the more the energy is required to meet the change in the structure, which leads to the larger latent heat.

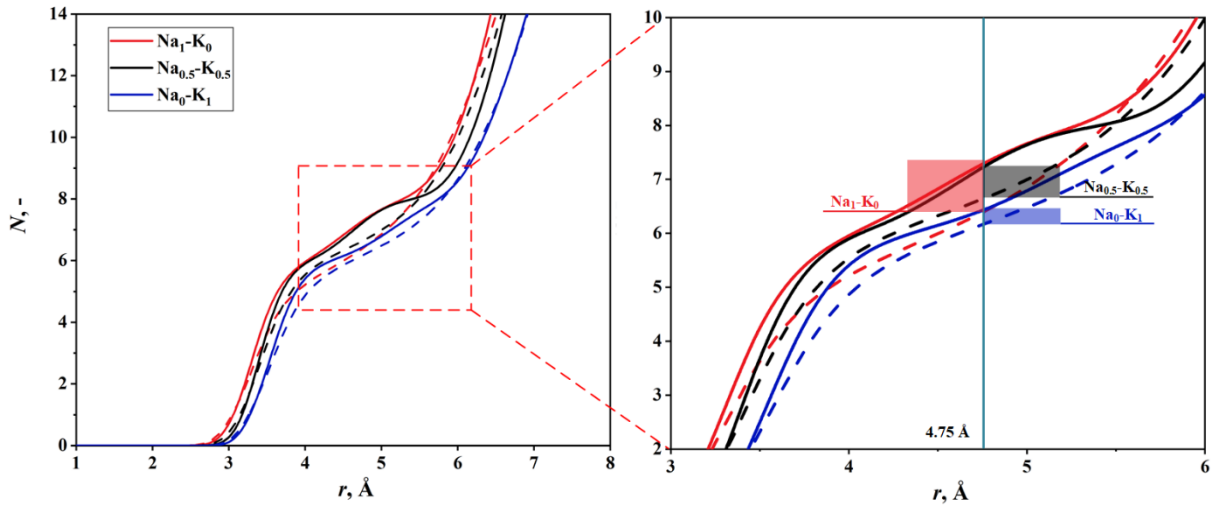


Figure 9. Coordination number curve of $\text{Na}_1\text{-K}_0$, $\text{Na}_{0.5}\text{-K}_{0.5}$, and $\text{Na}_0\text{-K}_1$. The solid line represents the coordination number curve “before melting” while the dashed line represents “after melting”. The temperature of “before melting” and “after melting” for $\text{Na}_1\text{-K}_0$, $\text{Na}_{0.5}\text{-K}_{0.5}$, and $\text{Na}_0\text{-K}_1$ is 580 K and 590 K, 490 K and 500 K, 600 K and 610 K respectively. The vertical line (4.75 Å) in the right figure indicates the first valley position of the radial distribution function. The height of the red, black and blue rectangular

represents the difference in the coordination number before/after melting for $\text{Na}_1\text{-K}_0$, $\text{Na}_{0.5}\text{-K}_{0.5}$, and $\text{Na}_0\text{-K}_1$ respectively.

5. Applications

From the above discussion, it can be concluded that mixing pure salts can decrease the melting point and does not impair the latent heat. It is very important for CSP plants on cloudy days and winter because the sunshine is not strong on these days. If the melting point of salt is too high, the weak sunshine cannot heat the salt to melt, so the energy storage through phase change cannot be achieved. In contrast, by using the low-melting-point eutectic, the concentrated solar energy is still possible to melt the salt. Thus, the application range of molten salt is extended and the energy storage efficiency is enhanced.

To test the extended application range of the salt mixture, two case studies were performed in Nottingham, UK and Dezhou, China. The latter is called the “Solar City of China”, where the 4th International Solar Cities Congress and Expo was held. The location of the two cities was shown in **Figure 10**(a) and (b).

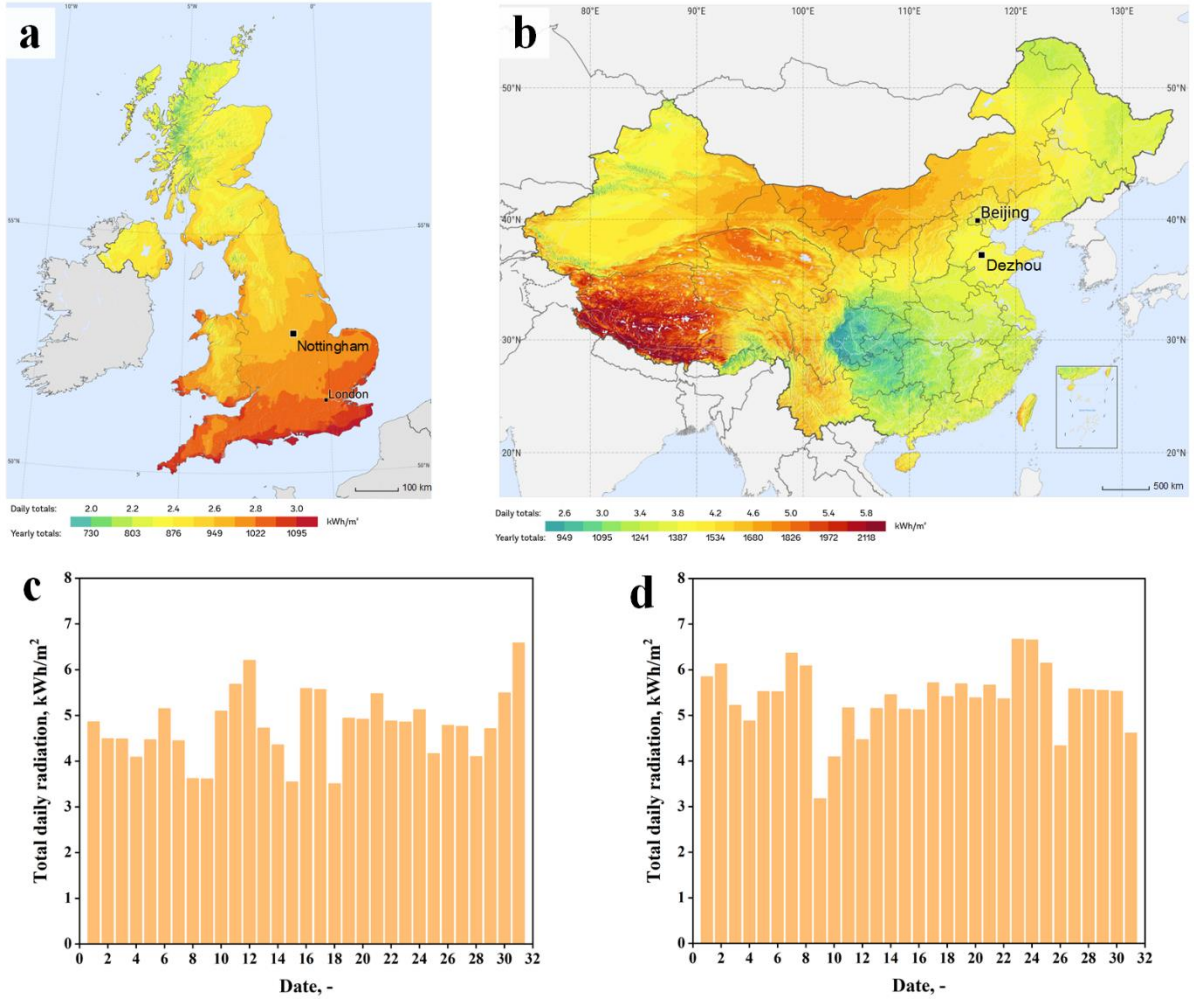


Figure 10. (a) - (b): Yearly average of global horizontal irradiation for the UK and China. Data from Ref. [36]. (c) - (d): Total daily radiation for Nottingham, UK and Dezhou, China, in July 2020.

The daily radiation is calculated by [37]:

$$H = K_T \cdot H_o \quad (10)$$

where K_T is the daily clearness index; H_o is the extraterrestrial radiation. H_o is computed by the following formula [38]:

$$H_o = (24/\pi)G_{SC} d_r [\cos(\varphi)\cos(\delta) \sin(w_s) + w_s \sin(\varphi)\sin(\delta)] \quad (11)$$

where G_{SC} is the solar constant = 1367 W/m²; d_r is the inverse relative distance between Earth and Sun, as defined by the following Eq. (12):

$$d_r = 1 + 0.033\cos(2\pi n / 365) \quad (12)$$

n is the n th day of the year; w_s is the sunset hour angle, as defined in Eq. (13):

$$\cos(w_s) = -\tan(\varnothing)\tan(\delta) \quad (13)$$

\varnothing is the latitude of the chosen city; δ is the solar declination angle, as defined by Eq. (14):

$$\delta = 23.45\sin[2\pi(284+n)/365] \quad (14)$$

The clearness index K_T is predicted by [39]:

$$K_T = k_{RS}(T_{max} - T_{min})^{0.5} \quad (15)$$

where T_{max} and T_{min} is the maximum and minimum temperature of each day; k_{RS} is the adjustment coefficient. Since Nottingham and Dezhou is the “interior region”, k_{RS} is taken as 0.16 [39].

Using Eqs. (10)-(15), the total daily radiation can be estimated. The results of July 2020 of the two cities are shown in Figure 10(c)-(d). The solar radiation shining on the CSP plants varies in one day, the total daily radiation is used as the data source for computing the hourly radiation.

The methodology for computing the total daily radiation takes into account the weather condition. The principle is that on cloudy days, at noon, some solar radiation is diffused by the cloud while in the evening, the cloud acts as a quilt to preserve heat; as a result, the ambient temperature difference is small. So, the effect of the weather condition can be reflected by the ambient temperature difference. For example, the weather on 23rd and 31st July in Dezhou are sunny and cloudy respectively; the recorded ambient temperature is 19°C~33°C and 24°C~31°C. It can be seen from Figure 10(d) that the computed total daily radiation of 23rd July is higher than that of 31st July, which is in agreement with the weather condition.

The daily radiation consists of direct beam radiation H_b and diffuse radiation H_d . Since only the direct beam radiation can be accepted by CSP plant, it is necessary to extract the diffuse radiation from the global radiation.

The daily diffuse radiation H_d is defined by the Erbs correlations [40]:

For $w_s \leq 81.4^\circ$

$$\begin{aligned}
H_d &= H \times (1 - 0.2727K_T + 2.4495K_T^2 - 11.951K_T^3 + 9.3879K_T^4), \quad \text{if } K_T < 0.715 \\
&= 0.143H, \quad \text{if } K_T \geq 0.715 \quad (16)
\end{aligned}$$

For $w_s > 81.4^\circ$

$$\begin{aligned}
H_d &= H \times (1 + 0.2832K_T - 2.557K_T^2 + 0.8448K_T^3), \quad \text{if } K_T < 0.715 \\
&= 0.175H, \quad \text{if } K_T \geq 0.715 \quad (17)
\end{aligned}$$

The following formula is adopted to calculate the hourly radiation I [40], which is related to the solar hour angle w :

$$I = H \times (\pi/24)[a + b\cos(w)]\{[\cos(w) - \cos(w_s)]/[\sin(w_s) - w_s\cos(w_s)]\} \quad (18)$$

where

$$a = 0.409 + 0.5016\sin(w_s - 60\pi/180) \quad (19)$$

$$b = 0.6609 - 0.4767\sin(w_s - 60\pi/180) \quad (20)$$

The hourly diffuse radiation is calculated by [41]:

$$I_d = H_d \times (\pi/24)\{[\cos(w) - \cos(w_s)]/[\sin(w_s) - w_s\cos(w_s)]\} \quad (21)$$

Finally, the hourly direct beam radiation I_b is obtained by extracting the diffuse radiation from the global radiation. The results for Nottingham are shown in **Figure 11(a)**. The direct beam radiation is used as the input of the CSP plant.

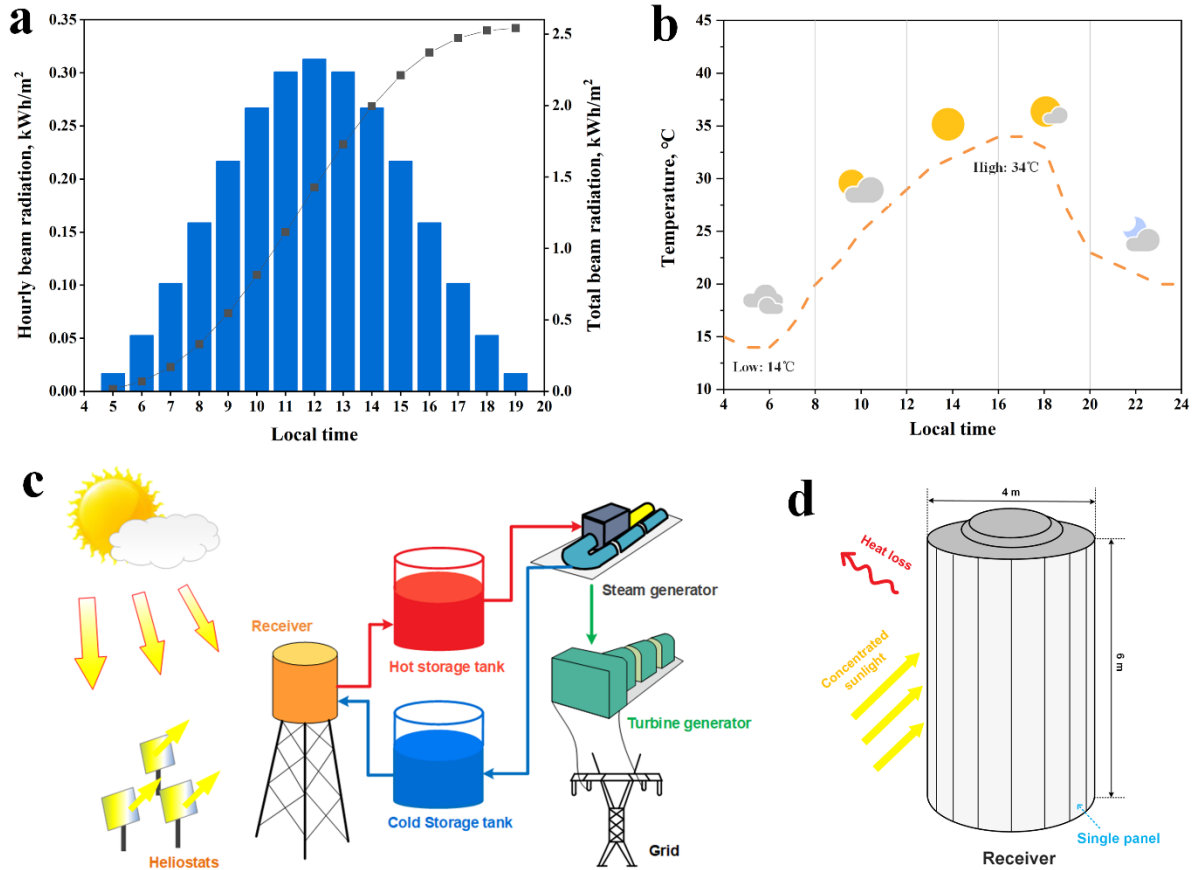


Figure 11. (a) Hourly direct beam radiation for Nottingham, UK on 31st July 2020. (b) Ambient temperature of Nottingham on 31st July 2020 [42]. (c) Typical solar tower power plant with thermal energy storage system used in the case study. (d) Schematic of the receiver.

A typical solar tower power plant used in the case study is shown in Figure 11(c). The plant is equipped with the thermal energy storage system, which enables operation at night. The schematic of the tubular external receiver is presented in Figure 11(d). This external receiver is designed based on Ref. [43]. It consists of several panels which comprise an array of tubes. Tubes in the same panel have fluid flows in the same direction. The tubes are arranged to shuttle the working fluid in multiple passes through the incident concentrated sunlight [44]. This structure effectively enhances heat transfer, like fins which increase the surface area.

Due to blocking, atmospheric attenuation, spillage, etc, not all the reflected solar radiation by heliostat can be received by the receiver [45]. An average optical efficiency η_{opt} , 0.6, is assumed in the case studies [46, 47]. So the hourly incident radiation on the receiver is:

$$q_{rev} = \eta_{opt} I_b A_{helio} N_{helio} \quad (22)$$

where A_{helio} is the surface area of a heliostat; N_{helio} is the number of the heliostat.

The heat loss consists of three parts: loss from receiver, pipeline and storage tank. The heat loss mechanism of the receiver includes radiation, convection and reflection:

$$q_{loss,rev} = q_{rad} + q_{cov} + q_{ref} \quad (23)$$

The radiative heat loss can be calculated by [17]:

$$q_{rad} = \epsilon \sigma (T_{rec,sur}^4 - T_{amb}^4) A_{rec,sur} Fr \quad (24)$$

where ϵ is the receiver surface emissivity; σ is the Boltzmann constant; $T_{rec,sur}$ and T_{amb} are the receiver surface temperature and ambient temperature respectively; $A_{rec,sur}$ is the receiver surface area; Fr is the view factor.

The heat loss due to the natural convection is [17]:

$$q_{nc} = h_{nc} (T_{rec,sur} - T_{amb}) A_{rec,sur} \quad (25)$$

$$h_{nc} = 0.81 (T_{rec,sur} - T_{amb})^{0.426} \quad (26)$$

The expression of the forced convection heat loss is given by:

$$q_{fc} = h_{fc} (T_{rec,sur} - T_{amb}) A_{rec,sur} \quad (27)$$

$$h_{fc} = \frac{Nu_{fc} k_{air}}{D_{rev}} \quad (28)$$

$$Nu_{fc} = 0.0287 Re_{fc}^{0.8} Pr_{air}^{1/3} \quad (29)$$

$$Re_{fc} = \frac{\rho_{air} v_{wind} D_{rec}}{\mu_{air}} \quad (30)$$

where ρ_{air} , μ_{air} , k_{air} and Pr_{air} are the density, dynamic viscosity, thermal conductivity and Prandtl number of air respectively; v_{wind} is the wind velocity, which is taken from Ref. [42, 48]; D_{rec} is the receiver diameter.

The heat loss due to the reflection is calculated by [17]:

$$q_{ref} = \omega \cdot q_{rev} \cdot Fr \quad (31)$$

where ω is the receiver surface absorptivity.

Since the pipelines and storage tanks are wrapped by insulation, the magnitude of the heat loss is small and is assumed as 2% of the absorbed energy.

In the two case studies, either $\text{Na}_{0.5}\text{-K}_{0.5}$ or pure KNO_3 is used as energy storage medium and heat transfer fluid. Properties of two salts are listed in **Table 3**.

Table 3

Properties of $\text{Na}_{0.5}\text{-K}_{0.5}$ and KNO_3

Property	$\text{Na}_{0.5}\text{-K}_{0.5}$	KNO_3
End melting point, °C	241.0	344.2
Density, g/cm ³	2.19	2.11
Thermal conductivity (solid), W/m K	0.74	0.69
Thermal conductivity (liquid), W/m K	0.53	0.48

A one-dimensional heat transfer model is used [49]:

$$\frac{\partial h}{\partial t} = \frac{\partial}{\partial x} \left(\alpha \frac{\partial h}{\partial x} \right) - \rho L \frac{\partial f}{\partial t} \quad (32)$$

where h is the sensible volumetric enthalpy; α is thermal diffusivity; f is liquid fraction. Designed configuration is listed in **Table 4**. The absorbed solar radiation of the receiver is converted into heat which is transferred to the hot storage tank, cold tank and pipeline.

During the simulation, the following assumptions are made: (1) the thermophysical properties of molten salts are independent of temperature; (2) molten salts are homogeneous and isotropic; (3) the sum of the inner volume of absorber tubes, pipelines and storage tanks is the same as the volume of molten salt, although in practical conditions, the former is larger to allow the thermal expansion; (4) the receiver is a uniform heater as it is shined by sunlight from various directions.

The boundary conditions are:

$$T_{\text{receiver, out}} = T_{\text{pipeline1, in}} \quad (33)$$

$$T_{\text{pipeline1, out}} = T_{\text{hot tank, in}} \quad (34)$$

$$T_{\text{hot tank, out}} = T_{\text{pipeline2, in}} \quad (35)$$

$$T_{\text{pipeline2, out}} = T_{\text{cold tank, in}} \quad (36)$$

where $T_{\text{receiver, out}}$, $T_{\text{pipeline1, out}}$, $T_{\text{hot tank, out}}$ and $T_{\text{pipeline2, out}}$ refer to the outlet temperature of the receiver, pipeline1, hot storage tank and pipeline2 respectively; $T_{\text{pipeline1, in}}$, $T_{\text{hot tank, in}}$ and $T_{\text{pipeline2, in}}$ and $T_{\text{cold tank, in}}$ refer to the inlet temperature of the pipeline1, hot storage tank, pipeline2 and cold storage tank respectively. Pipeline1 connects the receiver with the hot storage tank while Pipeline2 connects the hot storage tank with the cold storage tank.

The initial temperature of each component is the ambient temperature.

To solve Eq. (32), a fully implicit finite difference solution method is employed [49]. The time and space intervals are set as 1 hour and 1 m respectively. The finite difference equation is obtained by integrating the energy conservation equation over each control volume. The discretised equation is solved using the tridiagonal matrix algorithm (TDMA) iteration and the liquid fraction update method [50]. The convergence at a given time step is declared when the difference in the total enthalpy field is less than 10^{-5} .

Table 4

Designed parameters of the solar power tower system

Parameter	Value	Parameter	Value
Number of heliostat, -	1600	View factor, -	0.8
Surface of heliostat, m ²	54	Inner diameter of absorber tube, m	0.03
Optical efficiency, -	0.6	Length of absorber tube, m	1884
Height of receiver, m	6	Length of pipeline, m	300
Diameter of receiver, m	4	Inner diameter of pipeline, m	0.05
Surface area of receiver, m ²	75.4	Height of storage tank, m	10
Emissivity of receiver surface, -	0.88	Inner diameter of storage tank, m	3
Absorptivity of receiver surface, -	0.95		

The operability of the solar tower power plant in 2020 was tested. The result of Dezhou on 3rd December is shown in **Figure 12(a)-(b)**. The average temperature of the receiver T_{rec} rises with total absorbed solar radiation Q_{abs} . At noon, it increases sharply due to the strong solar radiation. At the same time, the total heat loss Q_{loss} becomes larger because of the serious reflection loss [17]. Although the reflection loss decreases in the afternoon, the radiation and convection loss becomes significant due to the large temperature difference with the environment. As a result, the hourly heat loss is still large. The sun sets at around 17:00 and T_{rec} no longer increases. The final value of T_{rec} using $\text{Na}_{0.5}\text{-K}_{0.5}$ exceeds the end melting point of $\text{Na}_{0.5}\text{-K}_{0.5}$, so the salt melts completely. In contrast, as seen in Figure 12(b), the final T_{rec} is lower than the melting point of KNO_3 , suggesting that the salt is still at the solid state. The receiver is blocked by solid salt, so this system cannot operate.

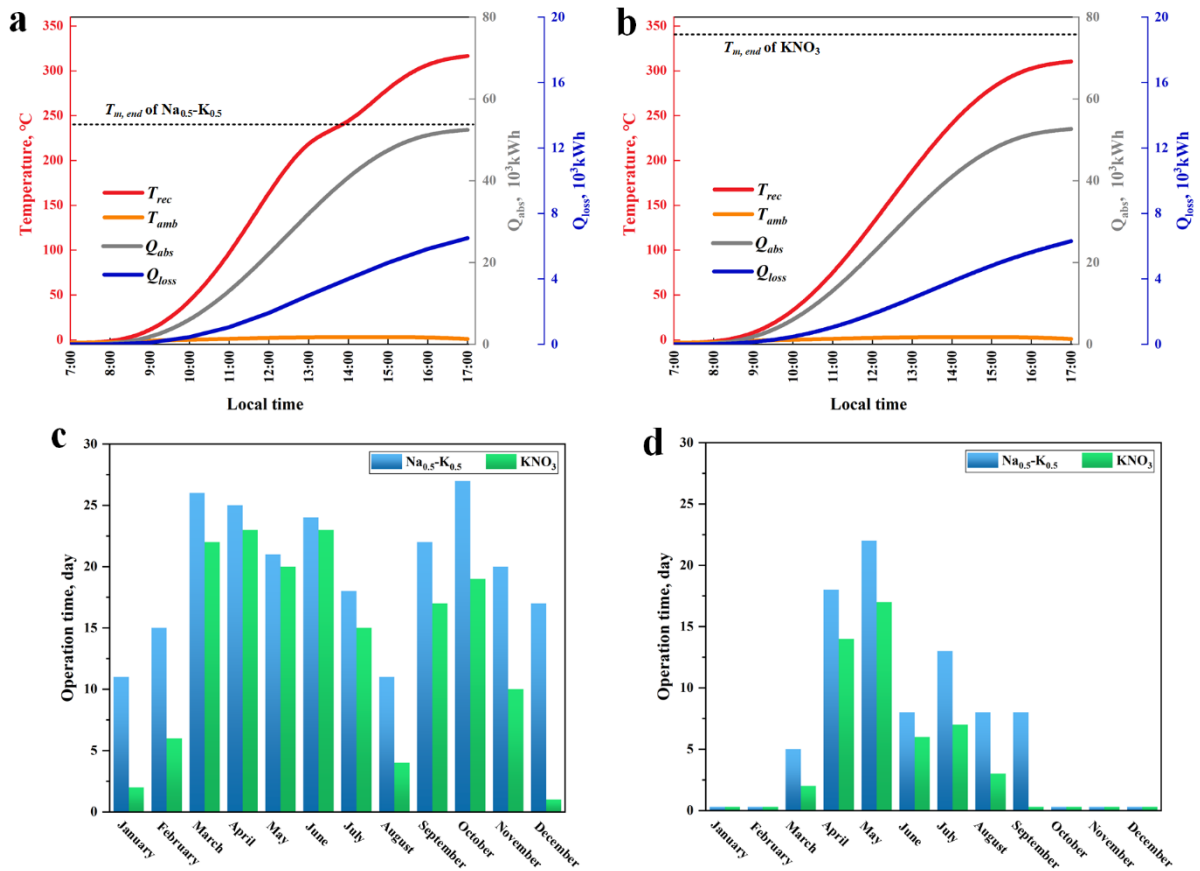


Figure 12. Receiver temperature T_{rec} , ambient temperature T_{amb} , total absorbed solar radiation Q_{abs} , and total heat loss Q_{loss} in the case study of Dezhou on 3rd December using (a) Na_{0.5}-K_{0.5} and (b) KNO₃ as energy storage medium. Monthly operation time of the solar power plant in (c) Dezhou and (d) Nottingham.

The operation of the power plant is assumed to start when all the salt melts and the temperature of the receiver inlet is 70°C higher than the melting point [51]. The operation time of the solar power plant in Dezhou and Nottingham was predicted, as **Figure 12(c)-(d)** shows. In the case study of Dezhou, the increase in operation time is evident in winter, i.e. December, January and February. As **Table 5** shows, by using the salt mixture, the yearly operation time of the plant is improved by 75 days for Dezhou and 33 days for Nottingham.

Table 5

Yearly operation time of the solar tower power plant using salt mixture or pure salt

City	Na _{0.5} -K _{0.5}	KNO ₃	Increase, day
Dezhou	237	162	75
Nottingham	82	49	33

6. Conclusions

Molten salts have been extensively used as heat transfer fluid and energy storage medium in solar thermal energy storage. However, their application is limited by “bad days” such as cloud days and winter because the sunlight is weak and the concentrated solar radiation cannot melt the salt. In the current study, the binary nitrate salt (NaNO₃-KNO₃) with different component ratios was tested and a molecular dynamics simulation was performed. The conclusions are summarised as follows:

(1) Through mixing pure salts, the melting point of molten salts can be decreased significantly while the latent heat is not impaired.

(2) The molecular simulation results indicate that low coulombic bonding energy accounts for the decreased melting point while the latent heat is correlated with the difference in coordination number before/after melting.

(3) The case study was performed in Dezhou and Nottingham in 2020. By using the salt mixture, the yearly operation time of the solar power plant is increased by 75 days (from 162 to 237 days) for Dezhou, and 33 days (from 49 to 82 days) for Nottingham.

(4) Mixing pure salts is proved to be a simple method to improve the utilization efficiency of the solar power plant system.

Acknowledgements

The authors would like to acknowledge the financial support by National Key R&D Program of China (No. 2018YFA0702300), H2020-MSCA-RISE-778104–ThermaSMART, Ningbo Science and Technology Bureau (No. 2019B10042), doctoral degree scholarship of China Scholarship Council (CSC). We are grateful for access to the University of Nottingham's Augusta HPC service.

Conflicts of interest

There are no conflicts to declare.

References

- [1] G. Alva, L. Liu, X. Huang, G. Fang, Thermal energy storage materials and systems for solar energy applications, *Renewable and Sustainable Energy Reviews*, 68 (2017) 693-706.
- [2] S. Zhang, D. Feng, L. Shi, L. Wang, Y. Jin, L. Tian, Z. Li, G. Wang, L. Zhao, Y. Yan, A review of phase change heat transfer in shape-stabilized phase change materials (ss-PCMs) based on porous supports for thermal energy storage, *Renewable and Sustainable Energy Reviews*, 135 (2021) 110127.
- [3] S. Bell, T. Steinberg, G. Will, Corrosion mechanisms in molten salt thermal energy storage for concentrating solar power, *Renewable and Sustainable Energy Reviews*, 114 (2019) 109328.
- [4] S. Zhang, Y. Jin, Y. Yan, Depression of melting point and latent heat of molten salts as inorganic phase change material: Size effect and mechanism, *Journal of Molecular Liquids*, 20 (2021) 117058.
- [5] Y. Lin, Y. Jia, G. Alva, G. Fang, Review on thermal conductivity enhancement, thermal properties and applications of phase change materials in thermal energy storage, *Renewable and Sustainable Energy Reviews*, 82 (2018) 2730-2742.
- [6] Q. Mao, Recent developments in geometrical configurations of thermal energy storage for concentrating solar power plant, *Renewable and Sustainable Energy Reviews*, 59 (2016) 320-327.
- [7] S.F. Ahmed, M. Khalid, W. Rashmi, A. Chan, K. Shahbaz, Recent progress in solar thermal energy storage using nanomaterials, *Renewable and Sustainable Energy Reviews*, 67 (2017) 450-460.
- [8] S. Zhang, Y. Yan, Melting and thermodynamic properties of nanoscale binary chloride salt as high-temperature energy storage material, *Case Studies in Thermal Engineering*, 25 (2021) 100973.

- [9] J. Ding, G. Pan, L. Du, J. Lu, W. Wang, X. Wei, J. Li, Molecular dynamics simulations of the local structures and transport properties of Na₂CO₃ and K₂CO₃, *Applied Energy*, 227 (2018) 555-563.
- [10] J. Ding, G. Pan, L. Du, J. Lu, X. Wei, J. Li, W. Wang, J. Yan, Theoretical prediction of the local structures and transport properties of binary alkali chloride salts for concentrating solar power, *Nano Energy*, 39 (2017) 380-389.
- [11] M. Chieruzzi, G.F. Cerritelli, A. Miliozzi, J.M. Kenny, L. Torre, Heat capacity of nanofluids for solar energy storage produced by dispersing oxide nanoparticles in nitrate salt mixture directly at high temperature, *Solar Energy Materials and Solar Cells*, 167 (2017) 60-69.
- [12] K. Coscia, S. Nelle, T. Elliott, S. Mohapatra, A. Oztekin, S. Neti, Thermophysical Properties of LiNO₃-NaNO₃-KNO₃ Mixtures for Use in Concentrated Solar Power, *Journal of Solar Energy Engineering*, 135 (2013).
- [13] A. Anagnostopoulos, A. Alexiadis, Y. Ding, Molecular dynamics simulation of solar salt (NaNO₃-KNO₃) mixtures, *Solar Energy Materials and Solar Cells*, 200 (2019) 109897.
- [14] M. Medrano, A. Gil, I. Martorell, X. Potau, L.F. Cabeza, State of the art on high-temperature thermal energy storage for power generation. Part 2—Case studies, *Renewable and Sustainable Energy Reviews*, 14 (2010) 56-72.
- [15] K.M. Powell, T.F. Edgar, Modeling and control of a solar thermal power plant with thermal energy storage, *Chemical Engineering Science*, 71 (2012) 138-145.
- [16] B. Grange, C. Dalet, Q. Falcoz, A. Ferrière, G. Flamant, Impact of thermal energy storage integration on the performance of a hybrid solar gas-turbine power plant, *Applied Thermal Engineering*, 105 (2016) 266-275.

- [17] S.S. Mostafavi Tehrani, R.A. Taylor, Off-design simulation and performance of molten salt cavity receivers in solar tower plants under realistic operational modes and control strategies, *Applied Energy*, 179 (2016) 698-715.
- [18] N. Khandelwal, M. Sharma, O. Singh, A.K. Shukla, Recent Developments in Integrated Solar Combined Cycle Power Plants, *Journal of Thermal Science*, 29 (2020) 298-322.
- [19] K. Neelam, S. Meeta, S. Onkar, S.A. Kumar, Thermo-economic analysis of an integrated solar thermal cycle (ISTC) using thermal storage, *Journal of Cleaner Production*, 320 (2021) 128725.
- [20] N. Khandelwal, M. Sharma, O. Singh, A. Kumar Shukla, Comparative analysis of the linear Fresnel reflector assisted solar cycle on the basis of heat transfer fluids, *Materials Today: Proceedings*, 38 (2021) 74-79.
- [21] S. Jayaraman, A.P. Thompson, O.A. von Lilienfeld, E.J. Maginn, Molecular simulation of the thermal and transport properties of three alkali nitrate salts, *Industrial & Engineering Chemistry Research*, 49 (2010) 559-571.
- [22] H. Ni, J. Wu, Z. Sun, G. Lu, J. Yu, Molecular simulation of the structure and physical properties of alkali nitrate salts for thermal energy storage, *Renewable Energy*, 136 (2019) 955-967.
- [23] G. Qiao, M. Lasfargues, A. Alexiadis, Y. Ding, Simulation and experimental study of the specific heat capacity of molten salt based nanofluids, *Applied Thermal Engineering*, 111 (2017) 1517-1522.
- [24] D. Chen, T.S. Totton, J.W.J. Akroyd, S. Mosbach, M. Kraft, Size-dependent melting of polycyclic aromatic hydrocarbon nano-clusters: A molecular dynamics study, *Carbon*, 67 (2014) 79-91.
- [25] G. Höhne, W.F. Hemminger, H.-J. Flammersheim, *Differential Scanning Calorimetry*, Springer-Verlag, Berlin, 2003.

- [26] H. Loulijat, H. Zerradi, S. Mizani, E.m. Achhal, A. Dezairi, S. Ouaskit, The behavior of the thermal conductivity near the melting temperature of copper nanoparticle, *Journal of Molecular Liquids*, 211 (2015) 695-704.
- [27] X. Xiao, P. Zhang, M. Li, Thermal characterization of nitrates and nitrates/expanded graphite mixture phase change materials for solar energy storage, *Energy Conversion and Management*, 73 (2013) 86-94.
- [28] K. Coscia, T. Elliott, S. Mohapatra, A. Oztekin, S. Neti, Binary and Ternary Nitrate Solar Heat Transfer Fluids, *Journal of Solar Energy Engineering*, 135 (2013).
- [29] X. Zhang, J. Tian, K. Xu, Y. Gao, Thermodynamic evaluation of phase equilibria in $\text{NaNO}_3\text{-KNO}_3$ system, *Journal of phase equilibria*, 24 (2003) 441-446.
- [30] W.D. Callister, *Fundamentals of materials Science and Engineering*, John Wiley & Sons, New York, 2001.
- [31] R.P. Feynman, R.B. Leighton, M. Sands, *The Feynman Lecture on Physics*, Addison Wesley Longman, Massachusetts, 1963.
- [32] D. Lee, B. Jo, Thermal energy storage characteristics of binary molten salt nanofluids: Specific heat and latent heat, *International Journal of Energy Research*, 45 (2021) 3231-3241.
- [33] A. Awad, H. Navarro, Y. Ding, D. Wen, Thermal-physical properties of nanoparticle-seeded nitrate molten salts, *Renewable Energy*, 120 (2018) 275-288.
- [34] P.D. Myers Jr, T.E. Alam, R. Kamal, D.Y. Goswami, E. Stefanakos, Nitrate salts doped with CuO nanoparticles for thermal energy storage with improved heat transfer, *Applied Energy*, 165 (2016) 225-233.
- [35] B.D. Iverson, S.T. Broome, A.M. Kruizenga, J.G. Cordaro, Thermal and mechanical properties of nitrate thermal storage salts in the solid-phase, *Solar Energy*, 86 (2012) 2897-2911.
- [36] SOLARGIS. Solar resource maps, <https://solargis.com/maps-and-gis-data/overview>, 2021.

- [37] H.L. Zhang, J. Baeyens, J. Degrève, G. Cacères, Concentrated solar power plants: Review and design methodology, *Renewable and Sustainable Energy Reviews*, 22 (2013) 466-481.
- [38] T. Pan, S. Wu, E. Dai, Y. Liu, Estimating the daily global solar radiation spatial distribution from diurnal temperature ranges over the Tibetan Plateau in China, *Applied Energy*, 107 (2013) 384-393.
- [39] E.J. Gago, S. Etxebarria, Y. Tham, Y. Aldali, T. Muneer, Inter-relationship between mean-daily irradiation and temperature, and decomposition models for hourly irradiation and temperature, *International Journal of Low-Carbon Technologies*, 6 (2011) 22-37.
- [40] Y. Tham, T. Muneer, B. Davison, Estimation of hourly averaged solar irradiation: evaluation of models, *Building Services Engineering Research and Technology*, 31 (2010) 9-25.
- [41] B.Y.H. Liu, R.C. Jordan, The interrelationship and characteristic distribution of direct, diffuse and total solar radiation, *Solar Energy*, 4 (1960) 1-19.
- [42] TIMEANDDATE. Nottingham history weather, <https://www.timeanddate.com/weather/uk/nottingham>, 2021.
- [43] Q. Zhang, D. Cao, Z. Ge, X. Du, Response characteristics of external receiver for concentrated solar power to disturbance during operation, *Applied Energy*, 278 (2020) 115709.
- [44] C.K. Ho, B.D. Iverson, Review of high-temperature central receiver designs for concentrating solar power, *Renewable and Sustainable Energy Reviews*, 29 (2014) 835-846.
- [45] Z. Yao, Z. Wang, Z. Lu, X. Wei, Modeling and simulation of the pioneer 1MW solar thermal central receiver system in China, *Renewable Energy*, 34 (2009) 2437-2446.
- [46] H.J. Lee, J.K. Kim, S.N. Lee, Y.H. Kang, Numerical study on optical performances of the first central-receiver solar thermal power plant in Korea, *Journal of Mechanical Science and Technology*, 30 (2016) 1911-1921.

- [47] Y.-L. He, F.-Q. Cui, Z.-D. Cheng, Z.-Y. Li, W.-Q. Tao, Numerical simulation of solar radiation transmission process for the solar tower power plant: From the heliostat field to the pressurized volumetric receiver, *Applied Thermal Engineering*, 61 (2013) 583-595.
- [48] Dezhou history weather, <http://www.tianqihoubao.com/lishi/dezhou/month/202007.html>, 2020.
- [49] M. Costa, D. Buddhi, A. Oliva, Numerical simulation of a latent heat thermal energy storage system with enhanced heat conduction, *Energy Conversion and Management*, 39 (1998) 319-330.
- [50] V.R. Voller, FAST IMPLICIT FINITE-DIFFERENCE METHOD FOR THE ANALYSIS OF PHASE CHANGE PROBLEMS, *Numerical Heat Transfer, Part B: Fundamentals*, 17 (1990) 155-169.
- [51] S.S.M. Tehrani, R.A. Taylor, P. Saberi, G. Diarce, Design and feasibility of high temperature shell and tube latent heat thermal energy storage system for solar thermal power plants, *Renewable Energy*, 96 (2016) 120-136.